

High-Resolution and Real-Time Three-Dimensional Imaging Algorithm With Envelopes of Spheres for UWB Radars

Shouhei Kidera, *Associate Member, IEEE*, Takuya Sakamoto, *Associate Member, IEEE*, and Toru Sato, *Member, IEEE*

Abstract—Ultrawideband pulse radars have a great potential for high-range resolution in near field imaging and can be used for noncontact measuring in precision or specular products such as reflector antennas and aircraft fuselages. We have already proposed a high-speed 3-D imaging algorithm, SEABED, which is based on a reversible transform, which is the boundary scattering transform, between the received signals and the target shape. However, the estimated image with SEABED is unstable with random noise because it utilizes a derivative of the received data. In this paper, we propose a robust 3-D imaging algorithm with an envelope of spheres that completely resolves the instability due to derivative operations. Moreover, to enhance the resolution of estimated images, this method is combined with a direct waveform compensation method that does not sacrifice high-speed calculation. Numerical simulations and an experiment confirm that the proposed method can realize fast, robust, and high-resolution 3-D imaging for arbitrary targets.

Index Terms—Direct waveform compensation, envelope of spheres, high-resolution and fast 3-D imaging, scattered waveform deformation, ultrawideband (UWB) pulse radars.

I. INTRODUCTION

VARIOUS measuring techniques require high-performance imaging systems with rapidness, robustness, accuracy, and high-resolution. Ultrawideband (UWB) pulse radars are promising candidates for these techniques. One of the applications of UWB radars is as a noncontact measurement for reflector antennas or aircraft bodies that have precision and specular surfaces. They can also be applied in target identification and self-localization systems for robots or vehicles. Although several different radar algorithms have been proposed, they either require intensive computation with optimizations [1]–[4] or have an insufficient spatial resolution to identify object shapes [5]–[7]. Contrarily, the high-speed 3-D

Manuscript received November 8, 2007; revised March 18, 2008. Current version published October 30, 2008. This work was supported in part by the 21st Century Center of Excellence Program under Grant 14213201, by the Grant-in-Aid for Scientific Research (A) under Grant 17206044, and by the Grant-in-Aid for Japan Society for the Promotion of Science Fellows under Grant 19-497.

The authors are with the Department of Communications and Computer Engineering, Graduate School of Informatics, Kyoto University, Kyoto 606-8501, Japan (e-mail: kidera@aso.cce.i.kyoto-u.ac.jp; t-sakamo@i.kyoto-u.ac.jp; tsato@kuee.kyoto-u.ac.jp).

Color versions of one or more of the figures in this paper are available online at <http://ieeexplore.ieee.org>.

Digital Object Identifier 10.1109/TGRS.2008.922319

imaging algorithm called Shape Estimation Algorithm based on BST and Extraction of Directly scattered waves (SEABED) [8], [9] achieves a direct and nonparametric imaging based on the reversible transforms, which are the boundary scattering transform (BST) and inverse BST (IBST), between the time delay and target boundary. The IBST has been used in geosurface measurements [10]–[12] and a breast cancer detection test [13]. Greenhalgh *et al.* make use of the IBST and signal amplitudes to obtain a reliable surface image. It has been verified that, in both cases, a direct and high-speed imaging of the assumed target is achieved. However, the estimated image using the IBST is unstable for noisy data because this transform uses the derivative of the received data.

Image stabilization methods based on adaptive smoothing have been proposed [14], [15]. However, there is a tradeoff between the resolution and stability due to the correlation length of the smoothing filters. To resolve this tradeoff, we have proposed a stable and fast 2-D imaging algorithm with an envelope of circles [16]. This method does not require derivative operations to create a stable image. In this paper, we extend this algorithm to the 3-D case. Our method calculates spheres with the observed delays for each antenna location and utilizes the principle that an arbitrary target boundary can be expressed as outer or inner envelopes of spheres. The method does not utilize derivative operations yet enables us to realize a robust imaging for arbitrary 3-D shapes.

In the case of a convex target, however, the estimated image around the target edge is distorted due to scattered waveform deformations. Waveform estimation (WE) for imaging has been proposed for high-resolution 2-D imaging [17], [18]. However, it requires long calculations for 3-D imaging due to the recursive WE procedures. To resolve this problem, we directly compensate the errors for the estimated delay with a spectrum offset correction (SOC) method. Numerical simulations and an experiment verify that the proposed method achieves a high-resolution, fast, and robust 3-D imaging for an arbitrary target shape.

II. CONVENTIONAL ALGORITHM

A. System Model

The upper part of Fig. 1 shows the system model. It assumes that the target has an arbitrary shape with a clear boundary and that the propagation speed of the radio wave is a known

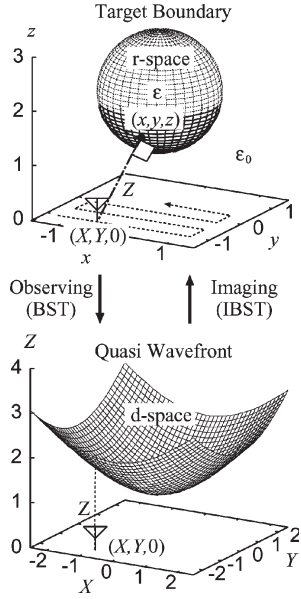


Fig. 1. Relationship between target boundary in r-space and quasi-wavefront in d-space.

constant. An omnidirectional antenna is scanned on the plane $z = 0$. We utilize a UWB pulse as the transmitting current and assume a linear polarization in the direction of the x -axis. R-space is defined as the real space where the target and the antenna are located and is expressed by the parameters x, y, z . These parameters are normalized by λ , which is the center wavelength of the pulse. We assume that $z > 0$ for simplicity. $s'(X, Y, Z')$ is defined as the received electric field at the antenna location $(x, y, z) = (X, Y, 0)$. $s(X, Y, Z')$ is defined as the output of the matched filter with the transmitted waveform, where $Z' = ct/(2\lambda)$ is expressed by the time t and the speed of the radio wave c . We connect the significant peaks of $s(X, Y, Z')$ as Z for each X and Y and call this surface (X, Y, Z) a quasi-wavefront. D-space is defined as the space expressed by (X, Y, Z) . The transform from d-space to r-space corresponds to the imaging that we deal with in this paper.

B. SEABED

We have already proposed a high-speed 3-D imaging algorithm known as SEABED, which utilizes a reversible transform BST between the point (x, y, z) in r-space and the point (X, Y, Z) in d-space. IBST is expressed as follows:

$$\left. \begin{aligned} x &= X - Z\partial Z/\partial X \\ y &= Y - Z\partial Z/\partial Y \\ z &= Z\sqrt{1 - (\partial Z/\partial X)^2 - (\partial Z/\partial Y)^2} \end{aligned} \right\}. \quad (1)$$

This transform gives us a strict solution for the assumed inverse problem and achieves a direct and nonparametric 3-D imaging. Fig. 1 shows the relationship between the target boundary and the quasi-wavefront. The estimated image with SEABED is, however, generally unstable with random noise because the derivative of the quasi-wavefront enhances the random errors.

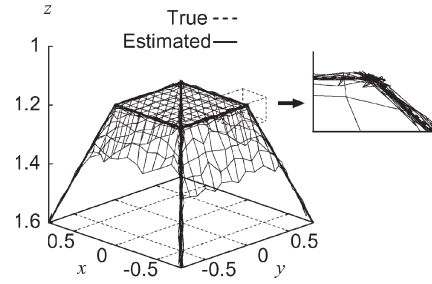


Fig. 2. Estimated image with SEABED for the convex target in noisy case where the adaptive smoothing is applied [(X, Y, Z) is known].

An example of the application of SEABED in noisy situations follows. We assume scanning the antenna in the range $-2.0\lambda \leq x \leq 2.0\lambda$, $-2.0\lambda \leq y \leq 2.0\lambda$ and calculate Z at 41 locations for each axis. A trapezoidal target boundary is assumed and a random value is added to each point of the true quasi-wavefront, the standard deviation of which is $5.0 \times 10^{-3}\lambda$, which corresponds to $S/N = 23$ dB [15]. To suppress the instability, an adaptive smoothing for the quasi-wavefront with the Gaussian filter has been proposed [14], where the optimum correlation length is approximated as $\sigma = \sqrt{\delta_{\max}Z/\pi}$ in the case of convex targets. Fig. 2 shows the estimated image with SEABED after adaptive smoothing has been applied. $\delta_{\max} = 0.1\lambda$ is empirically determined. Although this achieves a high-resolution image, instability still remains in the edge region of the estimated image. This is because the fluctuation of the quasi-wavefront cannot be suppressed completely and it still has the instability due to derivative operations. We also confirm that there is a tradeoff between stability and resolution due to data smoothing.

III. PROPOSED ALGORITHM

A. Target Boundary and Envelope of Spheres

To resolve the problem described in the previous section, we propose a robust 3-D imaging algorithm without derivative operations. This algorithm utilizes the principle that the target boundary can be expressed as the envelope of the spheres, with a center point $(X, Y, 0)$ and radius Z . Fig. 3 shows the relationship between the target boundary and the envelopes of the circles in a 2-D problem, for simplicity. Fig. 3 shows that the envelopes of the circles should circumscribe or inscribe to the target boundary, according to the sign of $\partial x/\partial X = 1 - Z\partial^2 Z/\partial X^2 - (\partial Z/\partial X)^2$, which denotes the target curvature [16]. For extension to a 3-D problem, we introduce the following proposition. Here, the sphere $S_{(X,Y,Z)}$ is defined as follows:

$$S_{(X,Y,Z)} = \{(x, y, z) | (x - X)^2 + (y - Y)^2 + z^2 < Z^2\}. \quad (2)$$

The point on a target surface (x, y, z) is defined as $\partial T_{(X,Y,Z)}$, which is transformed from (X, Y, Z) in (1).

Proposition 1: We define a part of the quasi-wavefront (X', Y', Z') as Γ_X , where Γ_X is a single-valued function for

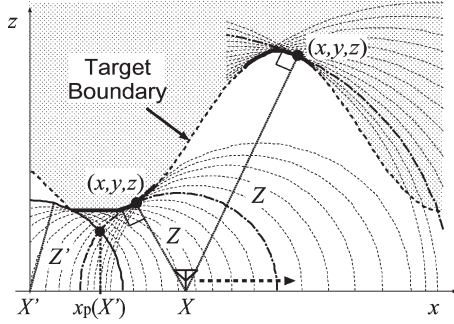


Fig. 3. Relationship between target boundary and envelopes of circles in 2-D problem.

X' and satisfies $Y' = Y$ and $(\partial Z'/\partial X')^2 + (\partial Z'/\partial Y')^2 \leq 1$. S_Y^1 and S_Y^{-1} are defined as follows:

$$\left. \begin{aligned} S_Y^1 &= \bigcup_{(X', Y, Z') \in \Gamma_X} S_{(X', Y, Z')} \\ S_Y^{-1} &= \bigcap_{(X', Y, Z') \in \Gamma_X} S_{(X', Y, Z')} \end{aligned} \right\}. \quad (3)$$

Now, the following relationship holds:

$$\partial T_{(X, Y, Z)} \subset \partial S_Y^{\nu_X}. \quad (4)$$

∂A expresses a boundary set of A , and $\nu_X = \text{sgn}(\partial x/\partial X)$ is defined.

The proof of Prop. 1 is given in Appendix A. This proposition should satisfy in the case of $X' = X$, and $\partial T_{(X, Y, Z)} \subset \partial S_X^{\nu_Y}$ holds, where $\nu_Y = \text{sgn}(\partial y/\partial Y)$, the part of the quasi-wavefront is defined as $(X', Y', Z') \in \Gamma_Y$, and

$$\left. \begin{aligned} S_X^1 &= \bigcup_{(X, Y', Z') \in \Gamma_Y} S_{(X, Y', Z')} \\ S_X^{-1} &= \bigcap_{(X, Y', Z') \in \Gamma_Y} S_{(X, Y', Z')} \end{aligned} \right\} \quad (5)$$

are defined. Now, (1) certifies $\partial T_{(X, Y, Z)} \neq \phi$, where ϕ is an empty set. Thus, $\partial T_{(X, Y, Z)}$ is expressed as follows:

$$\partial T_{(X, Y, Z)} \subset \partial S_Y^{\nu_X} \cap \partial S_X^{\nu_Y}. \quad (6)$$

Accordingly, a whole target boundary can be expressed as a sum set of $\partial T_{(X, Y, Z)}$ for $(X, Y, Z) \in \Gamma$, where Γ is the domain of (X, Y, Z) . Thus, the target boundary ∂T is expressed as follows:

$$\partial T \supset \bigcup_{(X, Y, Z) \in \Gamma} \partial T_{(X, Y, Z)}. \quad (7)$$

Here, ν_X and ν_Y denote whether the envelope of circles circumscribe or inscribe to the target boundary in each cross-section plane. The sign can be determined for each plane using the proposition in the 2-D model, which has been proved as Prop. 1 in [16].

With (6), each target region (x, y, z) for (X, Y, Z) is approximated as follows:

$$\left. \begin{aligned} \max_{\nu_X(X'-X)<0} x_p(X') \leq x \leq \min_{\nu_X(X'-X)>0} x_p(X') \\ \max_{\nu_Y(Y'-Y)<0} y_p(Y') \leq y \leq \min_{\nu_Y(Y'-Y)>0} y_p(Y') \\ z = \sqrt{Z^2 - (x-X)^2 - (y-Y)^2} \end{aligned} \right\} \quad (8)$$

where X' and Y' are searching variables. $x_p(X')$ is defined as the intersection point between the projective circle of $\partial S(X, Y, Z)$ and that of $\partial S(X', Y, Z')$ on the plane $y = Y$, as shown in Fig. 3. $y_p(Y')$ is similarly defined on the plane $x = X$. The derivation of (8) is given in Appendix B. The first and second equations in (8) estimate the target region along the x - and y -axes, respectively. The third equation estimates the target boundary as that of the spheres $\partial S_{(X, Y, Z)}$. Equation (8) determines an arbitrary target boundary without derivative operations. Thus, the instability caused by noise is suppressed.

B. Procedures for the Proposed Method

The procedures for the proposed method are as follows. $i = 0$ is set.

- Step 1) Obtain the output of the matched filter as $s(X, Y, Z')$ with received signals $s'(X, Y, Z')$ in each antenna location.
- Step 2) Extract quasi-wavefronts as (X, Y, Z'') , which satisfy

$$\begin{aligned} \partial s(X, Y, Z')/\partial Z' &= 0 \\ s(X, Y, Z') &\geq \alpha \max_{Z'} s(X, Y, Z'). \end{aligned} \quad (9)$$

Extract (X, Y, Z) as Γ_T from (X, Y, Z'') , which satisfies the local maximum of Z'' for each X and Y . Parameter α and the searching region of Z'' are determined empirically.

- Step 3) Remove interfered points from Γ_T , which have plural connecting candidates around themselves, and the remaining points are defined as Γ_i .
- Step 4) Select one point from Γ_i as (X_i, Y_i, Z_i) , and extract Γ_{X_i} and Γ_{Y_i} from each cross-section plane of Γ_i at $Y = Y_i$ and $X = X_i$, respectively.
- Step 5) Determine the signs of $\partial x/\partial X$ and $\partial y/\partial Y$ in Γ_{X_i} and Γ_{Y_i} , respectively.
- Step 6) Determine the target region as $\partial T_{(X_i, Y_i, Z_i)}$ by applying (8) with Γ_{X_i} and Γ_{Y_i} . Set $\Gamma_i = \Gamma_i/(X_i, Y_i, Z_i)$.
- Step 7) If Γ_i is not empty, set $i \leftarrow i + 1$ and return to Step 4). Otherwise, estimate the target boundary as $\partial T = \bigcup_{(X, Y, Z) \in \Gamma_0} \partial T_{(X, Y, Z)}$.

Fig. 4 shows the procedures for this method. The aforementioned method determines the target boundary as part of the envelope of spheres, and as such, we call it Envelope.

IV. STABILITY EVALUATIONS FOR ESTIMATED IMAGES IN NUMERICAL SIMULATIONS

A. Convex Boundary

In this section, imaging stability is evaluated as follows. Fig. 5 shows the estimated boundary with Envelope with the same quasi-wavefront used in Fig. 2. It can be seen that the image obtained has high resolution and a high degree of stability in the edge region of the target. This is because the proposed method enables us to transform the group of the quasi-wavefront to the group of the target boundary. Thus, it

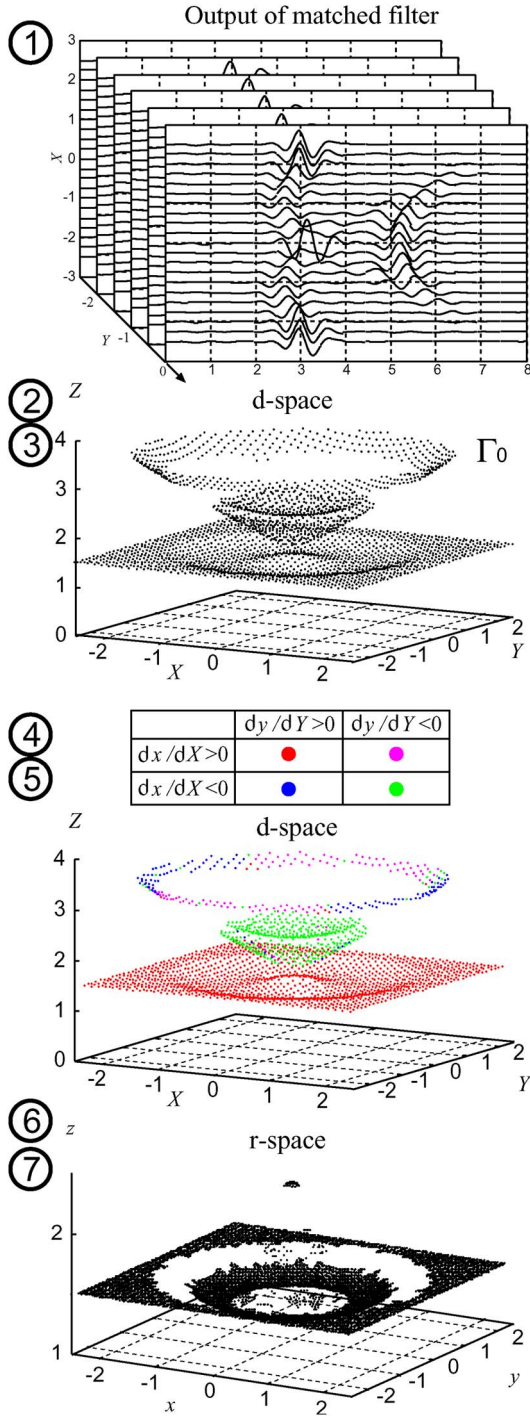


Fig. 4. Procedure of the proposed method.

resolves the tradeoff between stability and resolution due to data derivatives. We quantitatively evaluate the accuracy of each method, using an evaluation value μ that is defined as follows:

$$\mu = \sqrt{\frac{1}{N_T} \sum_{i=0}^{N_T} \min_x \|\mathbf{x} - \mathbf{x}_e^i\|^2} \quad (10)$$

where \mathbf{x} and \mathbf{x}_e^i express the location of the true target point and that of the estimated point, respectively. N_T is the total number

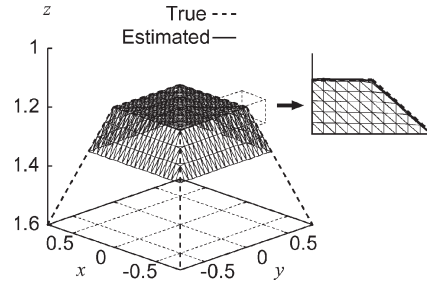


Fig. 5. Estimated image with Envelope for the convex target where the same quasi-wavefront in Fig. 2 is used.

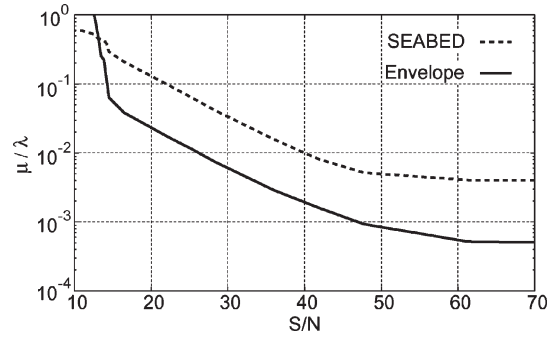


Fig. 6. Relationship between μ and S/N in the convex target [(X, Y, Z) is known].

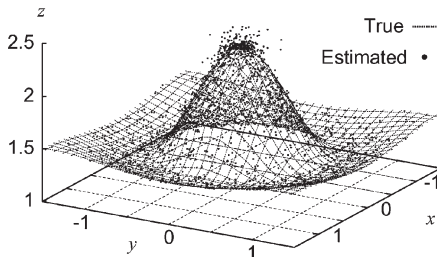


Fig. 7. Estimated image with SEABED for the concave target in noisy case [(X, Y, Z) is known].

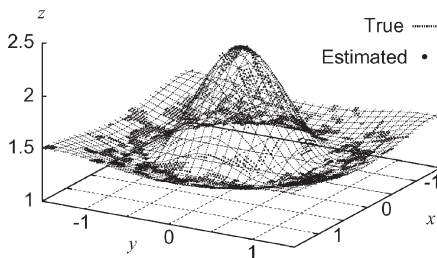


Fig. 8. Estimated image with Envelope for the concave target in noisy case [(X, Y, Z) is known].

of estimated points. Fig. 6 shows μ for the S/N in each method, where S/N is calculated as the standard deviation of Gaussian noises added to the true quasi-wavefront [15]. SEABED is combined with the adaptive filtering for the quasi-wavefront [14]. This figure confirms that Envelope has a significant advantage in producing stable accurate target imaging for $S/N \geq 13$ dB. For example, Envelope produces a five times improvement in μ compared to SEABED, where $S/N = 40$ dB.

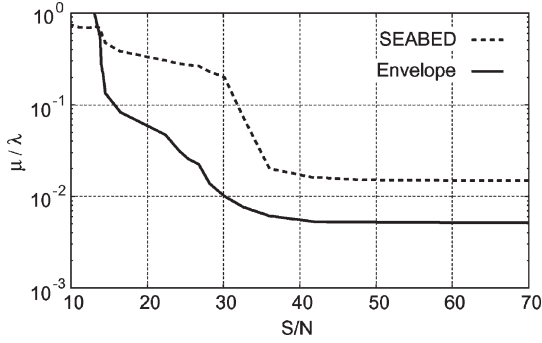


Fig. 9. Relationship between μ and S/N in the concave target [(X, Y, Z) is known].

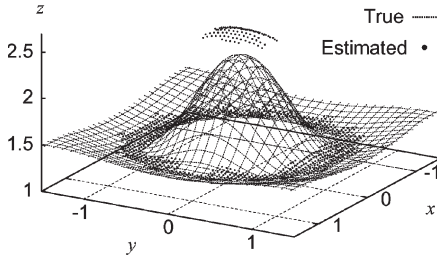


Fig. 10. Estimated image with Envelope for the concave target before phase compensations [(X, Y, Z) is unknown].

B. Concave Boundary

We now present the example applied to a concave target. We give random errors to the true quasi-wavefront, the standard deviation of which is $7.0 \times 10^{-3}\lambda$, which corresponds to $S/N = 24$ dB. The correlation length of the Gaussian filter is 0.1λ . Figs. 7 and 8 show the estimated images with SEABED and Envelope, respectively. We confirm that the image with SEABED is unstable, particularly around the concave region due to the derivative of the quasi-wavefront. Contrarily, the image with Envelope is quite stable for all regions of the target boundary and even for the noisy case. In addition, Fig. 9 shows the relationship between μ and the S/N for a concave target. This figure shows that μ in Envelope significantly improves compared to that in SEABED, where $S/N \geq 14$ dB. μ in Envelope is less than $1.0 \times 10^{-2}\lambda$ where $S/N \geq 30$ dB. These evaluations show that Envelope produces more stable images than SEABED for various target shapes.

V. HIGH-RESOLUTION IMAGING WITH DIRECT WAVEFORM COMPENSATIONS

A. Phase Rotation Compensation for Concave Boundaries

This section examines the proposed algorithm in more realistic situations with simulations using finite-difference time domain (FDTD) and a real experiment. Fig. 10 shows the estimated image for simulated data calculated by using the FDTD method. The received signals are observed at 41 locations along both the x - and y -axes where $-1.7\lambda \leq x$ and $y \leq 1.7\lambda$, respectively. The transmitted current is assumed to be a monocyclic pulse. We confirm that the estimated points with Envelope have large offset errors because the scattered wave from the concave boundaries has some phase rotation

TABLE I
RELATIONSHIP BETWEEN EACH SIGN OF $\partial x/\partial X$, $\partial y/\partial Y$ AND THE AMOUNT OF EACH PHASE ROTATION

	$\partial x/\partial X > 0$	$\partial x/\partial X < 0$
$\partial y/\partial Y > 0$	0	$\pi/2$
$\partial y/\partial Y < 0$	$\pi/2$	π

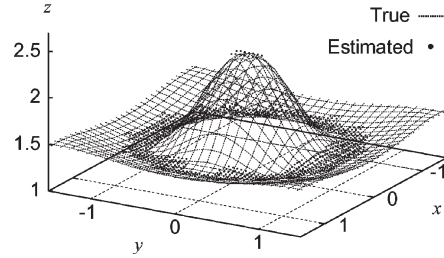


Fig. 11. Estimated image with Envelope for the concave target after phase compensations [(X, Y, Z) is unknown].

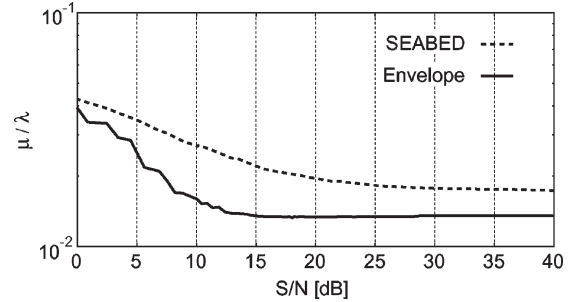


Fig. 12. Relationship between μ and S/N for the concave target [(X, Y, Z) is unknown].

from passing through the caustic points [19]. Here, the signs of $\partial x/\partial X$ and $\partial y/\partial Y$ correspond to the amount of phase rotation. Table I shows the relationship between the signs of $\partial x/\partial X$ and $\partial y/\partial Y$ and the phase rotations. If the signs of both $\partial x/\partial X$ and $\partial y/\partial Y$ are negative, the amount of phase rotation is π . In this method, we first calculate the range shift with each phase rotation of the transmitted waveform for $\pi/2$ and π and update Z for each group. Fig. 11 shows the estimated image after compensating for the phase rotations and verifies that the estimated image gives a more accurate target boundary. The computational time for this method is less than 0.1 s for a Xeon 3.2-GHz processor, which is suitable for real-time operations. Furthermore, a quantitative analysis of the accuracy in each method is presented later in this paper. Fig. 12 shows μ for the S/N in each algorithm. White noises are added to the received signals. In this case, S/N is defined as the ratio of peak instantaneous signal power to the averaged noise power after applying the matched filter. This figure confirms that Envelope significantly enhances μ for all S/N values. This is because the phase rotation caused by passing through a caustic can be robustly compensated without derivative operations, and μ in Envelope is enhanced with the accurate ranges.

B. Direct Range Compensations With Spectrum Shift Correction for Convex Boundaries

For convex targets, the estimated image with Envelope is usually distorted around the target edges or wedges. Fig. 13

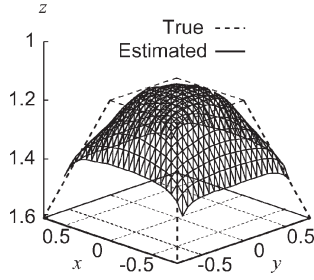


Fig. 13. Estimated image with Envelope for the convex target [(X, Y, Z) is unknown].

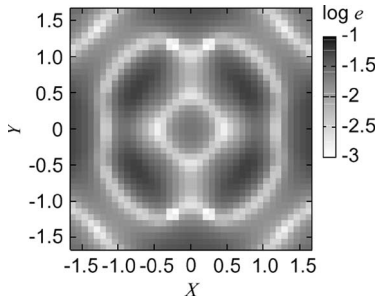


Fig. 14. Accuracy for quasi-wavefront with Envelope for the convex target.

shows the estimated image with Envelope for simulated data calculated by using the FDTD method. The image around the target edges is estimated as a smoothed surface, and the edge points cannot be identified. This is because the scattered waveform from the edge region is different to the transmitted one, and this causes a large error of the quasi-wavefront. Fig. 14 shows the accuracy of the quasi-wavefront for each antenna location. Here, $e = |Z_{\text{true}} - Z|$. For example, the antenna location at $(X, Y) = (-0.7\lambda, -0.7\lambda)$ receives strong echo from the edge. The error around the region is about $7.0 \times 10^{-2}\lambda/c$.

We have proposed a high-resolution imaging algorithm with shape and WEs, which is known as Envelope + WE, to enhance the resolution around the edge region [17], [18]. Using iterative procedures, this method updates matched filters in each step from the estimated waveform, which can be calculated with the previously extracted target boundary. Each scattered waveform can be quickly calculated by using the simplified Green's function integral. Fig. 15 shows the estimated image after two iterations of the shape and WE. We confirm that the resolution of the edge region remains inadequate, even if the number of iterations increases. The error around the edge region is about $3.0 \times 10^{-2}\lambda/c$. This is because the scattered wave includes negligible influence from the shadow region of the target and the effects of the polarimetry characteristic, which are not included in the simplified WEs. Moreover, the calculation time for this method is more than 10 s, which is not realistic for use in a real-time application.

To resolve these problems, we directly compensate for the range error with the center frequencies of the received waveforms. Fig. 16 shows the principle of the matched filter for the transmitted and scattered waveforms. We confirm that the matching point between the scattered and transmitted signals does not express the true time of arrival due to the waveform

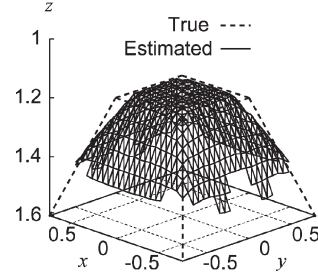


Fig. 15. Estimated image with Envelope + WE for the convex target [(X, Y, Z) is unknown].

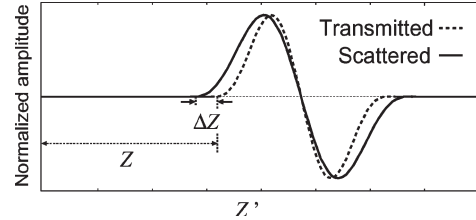


Fig. 16. Matching example between scattered and transmitted waveforms.

deformations. Here, we approximate the range shift ΔZ as follows:

$$\Delta Z = \frac{f_0}{W} (f_{\text{tr}}^{-1} - f_{\text{sc}}^{-1}) \quad (11)$$

where f_{tr} and f_{sc} are the center frequencies of the transmitted and scattered waveforms, respectively. $f_0 = c/\lambda$. W is a normalized constant determined with a fractional bandwidth of the transmitted signal. $W = 4$ is set. f_{sc} is calculated in the time domain as follows [20]:

$$f_{\text{sc}} = \frac{1}{2\pi L\Delta t} \angle \left(\sum_{i=0}^N s_i^* s_{i+L} \right) \quad (12)$$

where $s_i = s_{\text{sc}}(i\Delta t + 2Z\lambda/c)$, $s_{\text{sc}}(t)$ is an analytical signal of the scattered wave, Δt is the interval of the time sampling, and N is the total number of samples. Equation (12) enables us to calculate f_{sc} by eliminating the interferences from the multiple scattered or remaining direct waves because these components can be windowed in the time domain. Here, $N\Delta t$ and $L\Delta t$ are set to $1.0\lambda/c$ and $0.2\lambda/c$, respectively, which are empirically determined in terms of accurate and robust frequency estimation. The noise sensitivity for parameters N and L is presented at the frequency estimation in (12). The test signal is assumed to be the transmitted pulse used in the FDTD simulation. The frequency estimation error e_f is defined as $e_f = \sqrt{(1/M) \sum^M (f_{\text{est}} - f_{\text{true}})^2 / f_{\text{true}}^2}$, where f_{true} is the true center frequency of the test pulse and f_{est} is an estimated one in (12). M is the number of trials. The left- and right-hand sides of Fig. 17 show e_f for the S/N in each parameter $L\Delta t$ and $N\Delta t$, respectively, where the other parameter is fixed at $N\Delta t = 1.0\lambda/c$ and $L\Delta t = 0.2\lambda/c$, respectively. This figure shows that the parameters $L\Delta t$ and $N\Delta t$ should be around $0.2\lambda/c$ and $1.0\lambda/c$, respectively, to obtain a small e_f for the lower S/N . We call this algorithm Envelope + SOC.

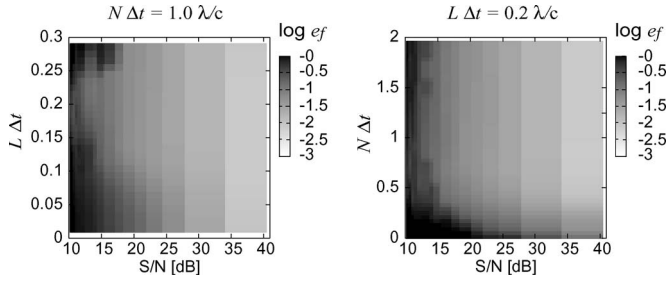


Fig. 17. Frequency estimation errors e_f in (12) for each parameter (left) $L\Delta t$, (right) $N\Delta t$, and S/N .

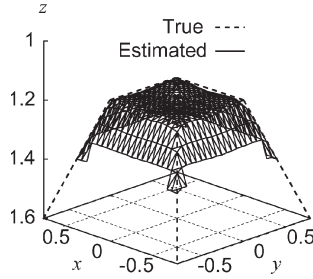


Fig. 18. Estimated image with Envelope + SOC for the convex target [(X, Y, Z) is unknown].

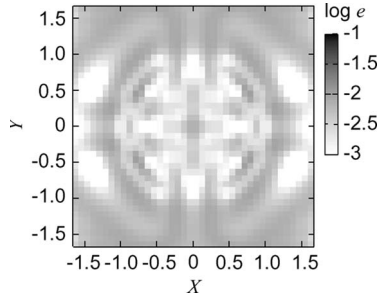


Fig. 19. Accuracy for quasi-wavefront with Envelope + SOC for the convex target.

C. Application Examples in Numerical Simulations

Figs. 18 and 19 show the estimated image and the accuracy for the quasi-wavefront, respectively, with Envelope + SOC. We confirm that our method achieves high-resolution 3-D imaging including the target edges and wedges. The error of the quasi-wavefront around this region is within $1.0 \times 10^{-2}\lambda/c$, and the calculation time for this method is 0.2 s for a Xeon 3.2-GHz processor. Here, we present the quantitative analysis for the resolution of the image obtained. We introduce mean curvature H as follows:

$$H = \frac{(1 + z_x^2)z_{yy} + (1 + z_y^2)z_{xx} - 2z_xz_yz_{xy}}{2(1 + z_x^2 + z_y^2)^{3/2}} \quad (13)$$

where $z_x = (\partial z / \partial x)$ and $z_{xy} = (\partial^2 z) / (\partial x \partial y)$ are defined. The left- and right-hand sides of Fig. 20 show the mean curvature H for both images with Envelope and Envelope + SOC, respectively. These results show that Envelope + SOC can reconstruct correct surfaces including edges and wedges, and it enhances the spatial resolution in terms of curvature.

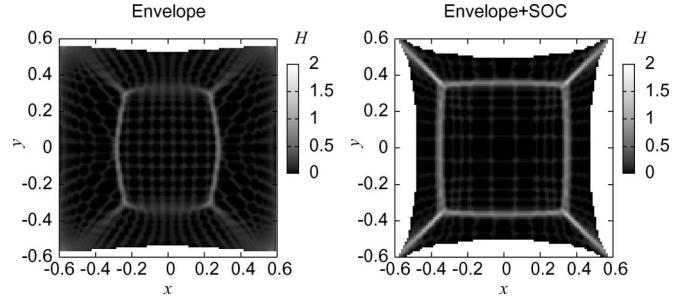


Fig. 20. Mean curvature H for the estimated images with (left) Envelope and (right) Envelope + SOC.

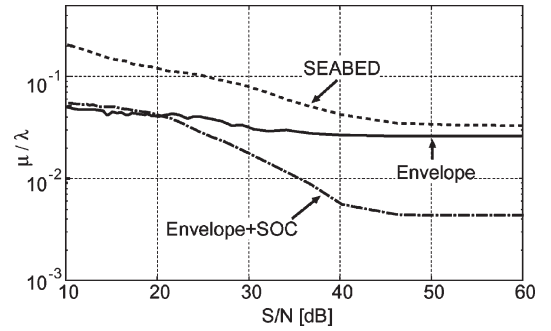


Fig. 21. Relationship between μ and S/N for the convex target [(X, Y, Z) is unknown].

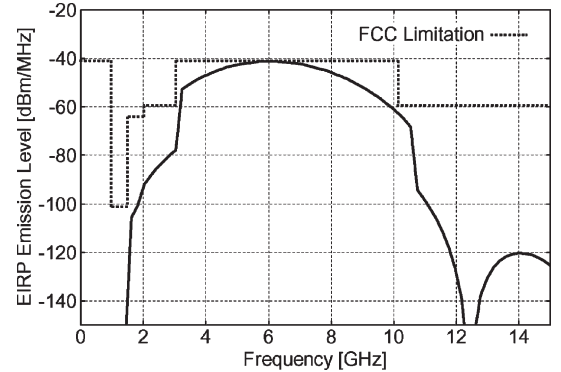


Fig. 22. EIRP emission level of the transmitted pulse within the released bandwidth of FCC in numerical simulation.

Here, μ for the S/N in each method is presented as follows. Fig. 21 shows the relationship between μ and the S/N for SEABED, Envelope, and Envelope + SOC. This figure shows that Envelope + SOC can enhance the accuracy $1.0 \times 10^{-2}\lambda$ where $S/N \geq 35$ dB. With a lower S/N , the accuracy with this method deteriorates as a result of the inaccuracy in the frequency estimation in (12). Enhancing the accuracy of the range compensation with a lower S/N is one of our future tasks.

Moreover, we have added a test case when the transmitted UWB signal is within the released bandwidth, which is regulated by the Federal Communication Commission (FCC). The FCC altered the equivalent isotropically radiated power (EIRP) for UWB signals within -41.3 dBm/MHz from 3.0 to 10.6 GHz. Fig. 22 shows the EIRP for the transmitted signal, which has been filtered with the released bandwidth. We have selected the center frequency of the monocyclic pulse as

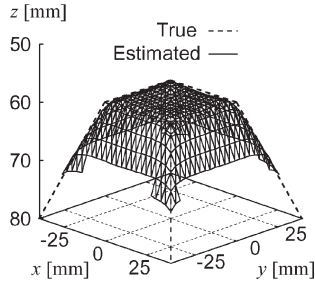


Fig. 23. Estimated image with Envelope + SOC with the regulated UWB signals in Fig. 22.

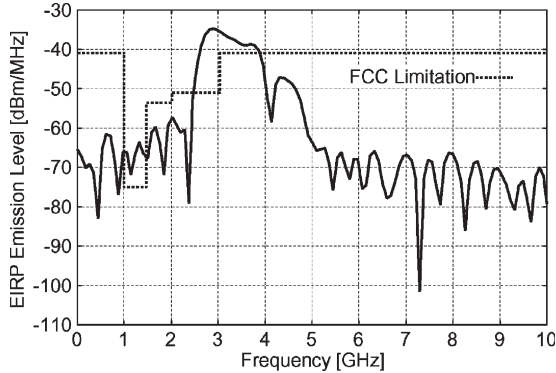


Fig. 24. EIRP emission level of the transmitted pulse used in the experiment.

6.0 GHz to retain the maximum signal power in the limited bandwidth. Fig. 23 shows the estimated image produced by Envelope + SOC with the regulated UWB signals. As shown in this figure, the estimated image is almost the same as that shown in Fig. 18. This result shows that the proposed algorithm can realize high-resolution 3-D imaging with the regulated UWB pulse. In addition, in this case, μ for Envelope + SOC is less than 0.5 mm, which is sufficiently accurate for the anticipated application thereof, i.e., as a noncontact measurement for reflector antennas or aircraft surfaces.

D. Application Example in Experiment

This section evaluates the performance from an experiment. We utilize a UWB pulse with a center frequency of 3.3 GHz and the 10-dB bandwidth of 2.0 GHz. Fig. 24 shows the EIRP of the transmitted signal used in the experiment. The distance between the transmitting and receiving antennas is 3.0 m, which is regulated by the environmental metric of the FCC [21]. Here, the receiving antenna gain is 2 dBi, and the loss of coaxial cable is 0.5 dB/m. As shown in Fig. 24, the UWB signal does not satisfy the bandwidth limitation of the FCC between 2.5 and 3.8 GHz. The maximum peak of the EIRP is -35.0 dB for 2.9 GHz. However, this experimental setup is in an anechoic chamber, where interferences to other communication signals are negligible. Also, even if the UWB signal power is limited with the released bandwidth, the proposed method can hold its performance by increasing the number of coherent integrations. The antenna has an elliptic polarization, of which the ratio of major to minor axis is about 17 dB, and the direction of the polarimetry axis of the antenna is along the y -axis. The 3-dB beamwidth of the antenna is about 90°. We use a trapezoid

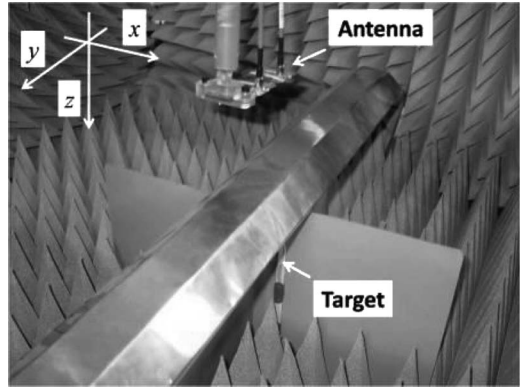


Fig. 25. Arrangement of the antennas and the target in the experiment.

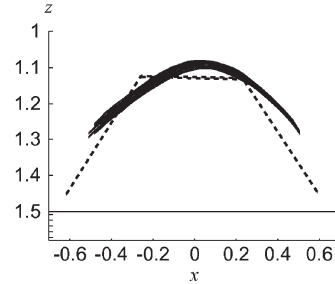
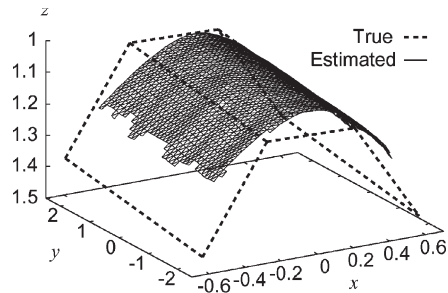


Fig. 26. Estimated image of Envelope in the experiment.

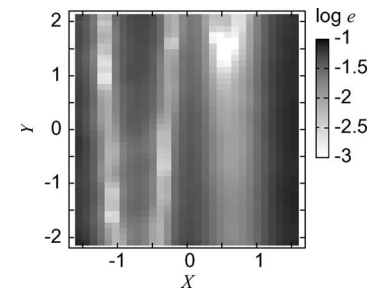


Fig. 27. Accuracy for the quasi-wavefront with Envelope method in the experiment.

target made from a stainless steel sheet. Fig. 25 shows the location of the antenna and the target. The transmitted and received antennas are scanned on the $z = 0$ plane for $-170 \text{ mm} \leq x \leq 170 \text{ mm}$ and $-200 \text{ mm} \leq y \leq 200 \text{ mm}$, respectively, where each sampling interval is set to 10 mm. The separation between the transmitted and received antennas is 48 mm in the y -direction. The data are coherently averaged 1024 times.

Figs. 26 and 27 show the estimated image and the accuracy for the quasi-wavefront, respectively, with Envelope. S/N is 35 dB. As shown in these figures, the resolution of the target

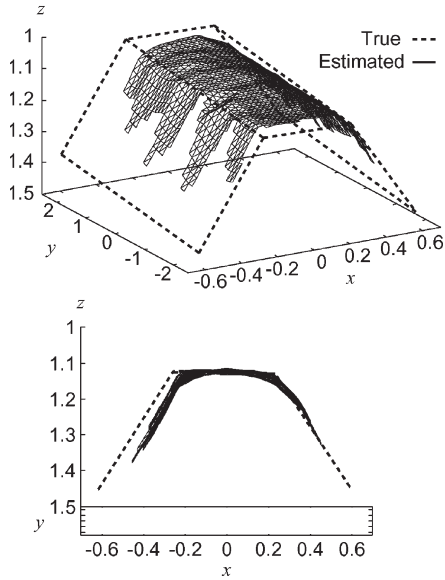


Fig. 28. Estimated image of Envelope + SOC in the experiment.

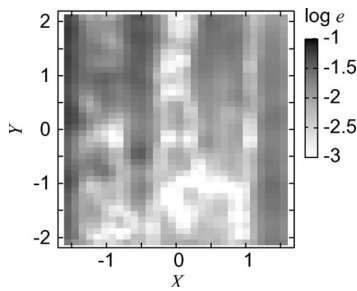


Fig. 29. Accuracy for the quasi-wavefront with Envelope + SOC in the experiment.

wedge is distorted due to the scattered waveform deformations. The μ defined in (10) from Envelope is $3.2 \times 10^{-2}\lambda$. Contrarily, Figs. 28 and 29 show the estimated image and the accuracy for the quasi-wavefront, respectively, with Envelope + SOC. These figures verify that Envelope + SOC can produce a higher resolution image around the wedges and the upper surface of the target with μ of $1.6 \times 10^{-2}\lambda$. However, there are some distortions in the estimated image compared to the results from the numerical simulations. This is because the fractional bandwidth of the experimental pulse is lower than that of the monocycle pulse. Thus, the scattered wave is severely interfered by the remains of the direct wave, which cannot be completely eliminated.

Moreover, the test case for a concave target is demonstrated as follows. Fig. 30 shows the arrangement of the antennas and the assumed object with a concave boundary. The S/N is 31 dB. Fig. 31 shows the true boundary of the concave target. The left- and right-hand sides of Fig. 32 show the estimated image and a cross-section view for $-0.1\lambda \leq x \leq 0.1\lambda$ with SEABED, respectively. Fig. 33 shows the same view with Envelope. These figures prove that Envelope produces a more stable boundary compared to the conventional SEABED. The accuracy distortions around the target edges for both methods are caused by the range errors due to the lower S/N . μ

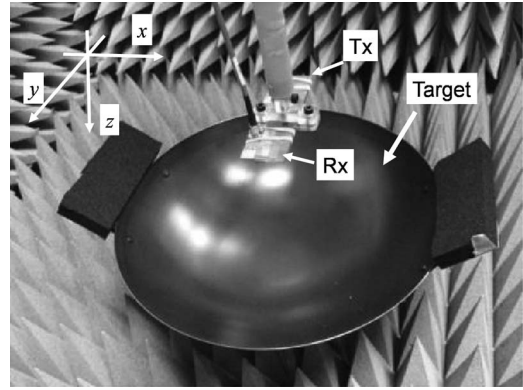


Fig. 30. Arrangement of the antennas and the concave target in the experiment.

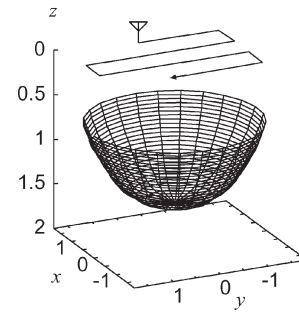


Fig. 31. True image for the concave target boundary in the experiment.

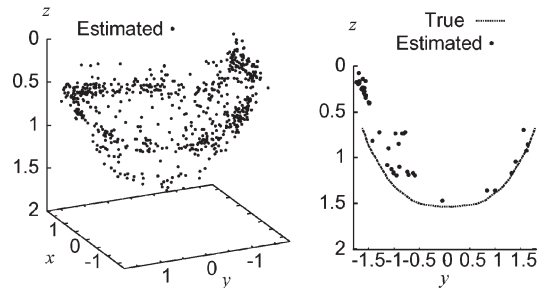


Fig. 32. (Left) Estimated 3-D image and (right) its cross section with SEABED for concave target in the experiment.

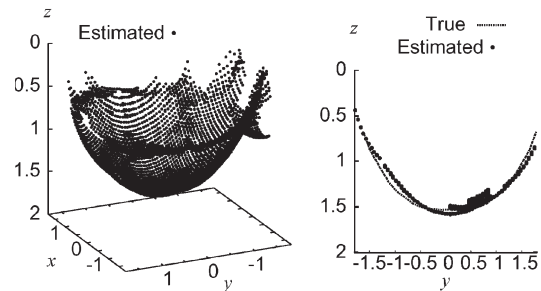


Fig. 33. (Left) Estimated 3-D image and (right) its cross section with Envelope for concave target in the experiment.

for SEABED and Envelope is $2.4 \times 10^{-1}\lambda$ and $1.4 \times 10^{-1}\lambda$, respectively. These experimental studies confirm that the proposed algorithm is superior with regard to stable high-resolution 3-D imaging for UWB radars.

VI. CONCLUSION

We have proposed Envelope, which is a fast and robust 3-D imaging algorithm with envelopes of spheres for an arbitrary target shape. It achieves a stable and high-resolution imaging without derivative operations. In addition, it realizes an accurate imaging for concave boundaries by compensating the phase rotations. Furthermore, to enhance the resolution of a convex target, we have introduced direct waveform compensations with SOC. The synthesis of Envelope and SOC realizes rapid and high-resolution 3-D imaging even in the edge region. The results from numerical simulations show that the accuracy for the quasi-wavefront is 1/100 center wavelength, and our method achieves a high-resolution 3-D imaging. The calculation time is 0.2 s for a Xeon 3.2-GHz processor, and thus, it can be used for real-time applications. We have also showed application examples with experimental data. These investigations verified that our proposed method achieves high-resolution and fast 3-D imaging even in a real environment. This algorithm can also be applied to multiple targets. The principle used in the proposed method can work even if each antenna receives multiple echoes from multiple scattering centers. However, it is difficult to retain the high-resolution 3-D imaging because the accuracy for SOC is distorted by waveform deformations due to the interfered echoes from the multiple targets. It is our important future work to resolve this problem.

APPENDIX A
PROOF OF PROPOSITION 1

Here, we utilize the following proposition, which has been proved as Prop. 2 in [16]. We define $x_{2d} = X - ZZ_X$ and $z_{2d} = Z\sqrt{1 - Z_X^2}$, and $\gamma_X = \{(X, Z) | (X, Y, Z) \in \Gamma_X\}$ is defined.

Proposition 2: If $\partial x_{2d}/\partial X > 0$ holds, for all $(X, Z) \in \gamma_X$, the following equation holds:

$$(x_{2d} - X)^2 + z_{2d}^2 \geq Z^2 \tag{14}$$

where an equal sign holds at only one point of (X, Z) .

Here, $x_{2d} = x$ and $z_{2d} = \sqrt{z^2 + (ZZ_Y)^2}$ holds from (1). By substituting x_{2d} and z_{2d} in (14)

$$(x - X)^2 + (ZZ_Y)^2 + z^2 \geq Z^2 \tag{15}$$

is obtained. Here, $y = Y - ZZ_Y$ holds in (1), and the next inequality holds

$$(x - X)^2 + (y - Y)^2 + z^2 \geq Z^2. \tag{16}$$

Fig. 34 shows the relationship between (x_{2d}, Y, z_{2d}) and (x, y, z) . According to Prop. 2, this relationship holds for all $(X', Y, Z') \in \Gamma_X$ because Y is constant and Γ_X corresponds to γ_X . Thus

$$\partial T_{(X,Y,Z)} \notin S_Y^1 \tag{17}$$

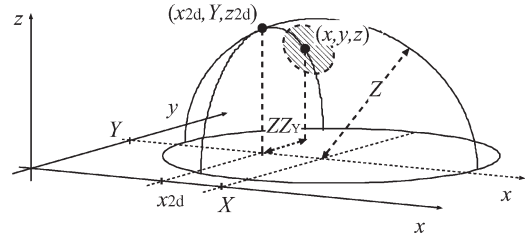


Fig. 34. Relationship between (x_{2d}, Y, z_{2d}) and (x, y, z) .

holds. Contrarily, only one element in $(X, Y, Z) \in \Gamma_X$ exists for (x, y, z) where it satisfies

$$(x - X)^2 + (y - Y)^2 + z^2 = Z^2. \tag{18}$$

Obviously, (17) and the aforementioned condition become the necessary and sufficient conditions that $(x, y, z) \in \partial S_Y^1$. In the case of $\partial x/\partial X < 0$, $(x, y, z) \in \partial S_Y^{-1}$ can be proved by using a similar approach, and Prop. 1 has been proved.

APPENDIX B
DERIVATION OF (8)

Here, $\partial x/\partial X > 0$ and $\partial y/\partial Y < 0$ are assumed for the quasi-wavefronts $(X', Y, Z') \in \Gamma_X$ and $(X, Y', Z'') \in \Gamma_Y$, respectively. With Prop. 1, the following inequalities hold:

$$(x - X')^2 + (y - Y)^2 + z^2 > Z'^2, \quad (X' \neq X) \tag{19}$$

$$(x - X)^2 + (y - Y')^2 + z^2 < Z''^2, \quad (Y' \neq Y). \tag{20}$$

With the aforementioned equations and (18), the following relationships hold:

$$\left. \begin{aligned} x &< \frac{X+X'}{2} - \frac{Z'^2-Z^2}{2(X'-X)}, & (X' > X) \\ x &> \frac{X+X'}{2} - \frac{Z'^2-Z^2}{2(X'-X)}, & (X' < X) \\ y &< \frac{Y+Y'}{2} - \frac{Z''^2-Z^2}{2(Y'-Y)}, & (Y' > Y) \\ y &> \frac{Y+Y'}{2} - \frac{Z''^2-Z^2}{2(Y'-Y)}, & (Y' < Y) \end{aligned} \right\}. \tag{21}$$

Here, these inequalities are equivalent to the first and second terms of (8) in the case where $\nu_X = 1$ and $\nu_Y = -1$. Similarly, for each combination of the signs of $\partial x/\partial X$ and $\partial y/\partial Y$, (8) is derived.

REFERENCES

- [1] A. Massa, D. Franceschini, G. Franceschini, M. Pastorino, M. Raffetto, and M. Donelli, "Parallel GA-based approach for microwave imaging applications," *IEEE Trans. Antennas Propag.*, vol. 53, no. 10, pp. 3118–3127, Oct. 2005.
- [2] C. Chiu, C. Li, and W. Chan, "Image reconstruction of a buried conductor by the genetic algorithm," *IEICE Trans. Electron.*, vol. E84-C, no. 12, pp. 1946–1951, Dec. 2001.
- [3] J. Song, Q. H. Liu, P. Torrione, and L. Collins, "Two-dimensional and three dimensional NUFFT migration method for landmine detection using ground-penetrating radar," *IEEE Trans. Geosci. Remote Sens.*, vol. 44, no. 6, pp. 1462–1469, Jun. 2006.
- [4] T. Sato, T. Wakayama, and K. Takemura, "An imaging algorithm of objects embedded in a lossy-dispersive medium for subsurface radar-data processing," *IEEE Trans. Geosci. Remote Sens.*, vol. 38, no. 1, pp. 296–303, Jan. 2000.
- [5] D. Liu, G. Kang, L. Li, Y. Chen, S. Vasudevan, W. Joines, Q. H. Liu, J. Krolik, and L. Carin, "Electromagnetic time-reversal imaging of a target in a cluttered environment," *IEEE Trans. Antennas Propag.*, vol. 53, no. 9, pp. 3058–3066, Sep. 2005.

- [6] D. Liu, J. Krolik, and L. Carin, "Electromagnetic target detection in uncertain media: Time-reversal and minimum-variance algorithms," *IEEE Trans. Geosci. Remote Sens.*, vol. 45, no. 4, pp. 934–944, Apr. 2007.
- [7] Q. Zhang, T. S. Yeo, H. S. Tan, and Y. Luo, "Imaging of a moving target with rotating parts based on the Hough transform," *IEEE Trans. Geosci. Remote Sens.*, vol. 46, no. 1, pp. 291–299, Jan. 2008.
- [8] T. Sakamoto and T. Sato, "A target shape estimation algorithm for pulse radar systems based on boundary scattering transform," *IEICE Trans. Commun.*, vol. E87-B, no. 5, pp. 1357–1365, May 2004.
- [9] T. Sakamoto, "A fast algorithm for 3-dimensional imaging with UWB pulse radar systems," *IEICE Trans. Commun.*, vol. E90-B, no. 3, pp. 636–644, Mar. 2007.
- [10] S. A. Greenhalgh and L. Marescot, "Modeling and migration of 2-D georadar data: A stationary phase approach," *IEEE Trans. Geosci. Remote Sens.*, vol. 44, no. 9, pp. 2421–2429, Sep. 2006.
- [11] T. Sakamoto, S. Kidera, and T. Sato, "SEABED algorithm and comments on 'Modeling and Migration of 2-D georadar data: A stationary phase approach'," *IEEE Trans. Geosci. Remote Sens.*, vol. 45, no. 10, p. 3300, Oct. 2007.
- [12] S. A. Greenhalgh and L. Marescot, "Authors' reply to comments by Takuya Sakamoto, Shouhei Kidera, and Toru Sato on 'SEABED algorithm and comments on 'Modeling and migration of 2-D georadar data: A stationary phase approach'," *IEEE Trans. Geosci. Remote Sens.*, vol. 46, no. 1, p. 300, Jan. 2008.
- [13] M. Converse, E. J. Bond, B. D. Van Veen, and S. C. Hagness, "A computational study of ultra-wideband versus narrowband microwave hyperthermia for breast cancer treatment," *IEEE Trans. Microw. Theory Tech.*, vol. 54, no. 5, pp. 2169–2180, May 2006.
- [14] T. Sakamoto, S. Kidera, T. Sato, and S. Sugino, "An experimental study on a fast 3-D imaging algorithm for UWB pulse radars," *IEICE Trans. Commun.*, vol. J90-B, no. 1, pp. 66–73, Jan. 2007. (in Japanese).
- [15] T. Sakamoto and T. Sato, "A 2-D image stabilization algorithm for UWB pulse radars with fractional boundary scattering transform," *IEICE Trans. Commun.*, vol. E90-B, no. 1, pp. 131–139, Jan. 2007.
- [16] S. Kidera, T. Sakamoto, and T. Sato, "A robust and fast imaging algorithm with an envelope of circles for UWB pulse radars," *IEICE Trans. Commun.*, vol. E90-B, no. 7, pp. 1801–1809, Jul. 2007.
- [17] S. Kidera, T. Sakamoto, T. Sato, and S. Sugino, "An accurate imaging algorithm with scattered waveform estimation for UWB pulse radars," *IEICE Trans. Commun.*, vol. E89-B, no. 9, pp. 2588–2595, Sep. 2006.
- [18] S. Kidera, T. Sakamoto, and T. Sato, "A high-resolution imaging algorithm without derivatives based on waveform estimation for UWB radars," *IEICE Trans. Commun.*, vol. E90-B, no. 6, pp. 1487–1494, Jun. 2007.
- [19] T. Sakamoto and T. Sato, "A phase compensation algorithm for high-resolution pulse radar systems," *IEICE Trans. Commun.*, vol. E87-B, no. 6, pp. 1631–1638, 2004.
- [20] K. Nishimura, T. Sato, T. Nakamura, and M. Ueda, "High sensitivity radar-optical observations of faint meteors," *IEICE Trans. Commun.*, vol. E84-C, no. 12, pp. 1877–1884, Dec. 2001.
- [21] R. Aiello and A. Batra, *Ultra Wideband Systems, Technologies and Applications*. London, U.K.: Newnes Publication, 2006, pp. 17–52.



Shouhei Kidera (S'05–A'07) received the B.E. degree from Kyoto University, Kyoto, Japan, in 2003 and the M.E. and Ph.D. degrees from the Graduate School of Informatics, Kyoto University, in 2005 and 2007, respectively.

He is currently a Research Fellow of the Japan Society for the Promotion of Science with the Department of Communications and Computer Engineering, Graduate School of Informatics, Kyoto University. His current research interest is in signal processing for ultrawideband radars.

Dr. Kidera is a member of the Institute of Electronics, Information, and Communication Engineers of Japan and the Institute of Electrical Engineering of Japan.



Takuya Sakamoto (S'04–A'05) was born in Nara, Japan, in 1977. He received the B.E. degree from Kyoto University, Kyoto, Japan, in 2000, and the M.I. and Ph.D. degrees from the Graduate School of Informatics, Kyoto University, in 2002 and 2005, respectively.

He is an Assistant Professor with the Department of Communications and Computer Engineering, Graduate School of Informatics, Kyoto University. His current research interest is in signal processing for ultrawideband pulse radars.

Dr. Sakamoto is a member of the Institute of Electronics, Information, and Communication Engineers of Japan and the Institute of Electrical Engineering of Japan.



Toru Sato (M'92) received the B.E., M.E., and Ph.D. degrees in electrical engineering from Kyoto University, Kyoto, Japan, in 1976, 1978, and 1982, respectively.

He has been with Kyoto University since 1983, where he is currently a Professor with the Department of Communications and Computer Engineering, Graduate School of Informatics. His major research interests include system design and signal processing aspects of atmospheric radars, radar remote sensing of the atmosphere, observations of precipitation using radar and satellite signals, radar observation of space debris, and signal processing for subsurface radar signals.

Dr. Sato is the recipient of the Tanakadate Prize in 1986. He is a Fellow of the Institute of Electronics, Information, and Communication Engineers of Japan, the Society of Geomagnetism and Earth, Planetary and Space Sciences, the Japan Society for Aeronautical and Space Sciences, and the American Meteorological Society.